Regenerating axons and blood vessels in tissue engineered scaffolds have defined spatial relationships after spinal cord injury.

Running title: Spatial relationships of axons and vessels

Ahad M. Siddiqui, PhD[1]*; Priska Summer, M.D.[2]*; David Oswald, M.D.[2]*; Domnhall Kelly, M.Sc.[3]; Jeffrey Hakim, Ph.D.[1]; Bingkun Chen, M.B.A., Ph.D[1].; Michael J. Yaszemski, M.D., Ph.D.[4]; Anthony J. Windebank, M.D.[1]; Nicolas N. Madigan, MB, BCh, BAO, PhD[1]

* denotes equal contribution

[1] Dept. of Neurology, Mayo Clinic, Rochester, Minnesota, United States

[2] Paracelsus Medical University of Salzburg, Austria

[3] National University of Ireland Galway, Galway, Ireland

[4] Dept. of Orthopedic Surgery, Mayo Clinic, Rochester, Minnesota, Unites States

Corresponding Author: Dr. Nicolas N. Madigan, Department of Neurology, Mayo Clinic, 200 First Street SW, Rochester, MN 55905. E-mail: madigan.nicolas@mayo.edu

Number of Pages: 44

Number of Figures: 7

Number of Words: (i) Body: 5404 (ii) Abstract: 348

Grant Support: This work was generously funded by grants from the National Institute of Biomedical Imagining and Bioengineering (EB02390), National Institute of Biomedical Imagining and Bioengineering (TL1 TR002380), Morton Cure Paralysis Fund, and Craig H. Nielsen Foundation.

Abstract

Spinal cord injury (SCI) results in lifelong paralysis due to the poor regenerative capability of the central nervous system and the hostile microenvironment that is created from processes such as inflammation, scarring, axonal dieback, and demyelination. Hydrogel scaffolds facilitate a permissive regenerative environment and overcome these barriers by reducing scarring. One important other consideration for axonal regeneration is the availability of nutrients and oxygen, making it crucial to further investigate vascularization characteristics in the regenerating spinal cord.

We previously described the close relationship between blood vessel formation and axonal regeneration. In this study, we focused on identifying the vascular – axonal relationship, as well describing novel techniques to analyze their interactions after a complete T9 spinal cord transection in rats. Following implantation of positively charged oligo-polyethylene glycol fumarate (OPF+) scaffolds containing Matrigel-only (MG), Schwann cells (SCs), or SCs with rapamycin-eluting poly-lactic-co-glycolic acid (PLGA) microspheres (RAPA), stereological methods were applied to measure core area, blood vessel number, volume, diameter, inter-vessel distances, total vessel surface and cross-sectional areas, and radial diffusion distances in each group 6 weeks after implantation.

Immuno-histochemical and stereological analysis demonstrated a significantly larger core area in the RAPA group and found a total of 2,494 myelinated and 4,173 unmyelinated axons at 10 micron circumferential intervals around 708 individual blood vessel profiles within scaffold channels. We found that axon number and surface density in the SC group exceeded that seen in the MG and RAPA groups and that higher axonal densities correlated with smaller vessel cross-sectional areas. Generally, axons were concentrated within a concentric distance of 200 microns

from the blood vessel wall, but were excluded from a 25 micron zone immediately adjacent to the vessel. Using a statistical spatial algorithm to generate cumulative distribution functions of axons within each scaffold channel type, we demonstrated that axons located around blood vessels were not randomly distributed.

By providing methods to quantify the axonal-vessel relationship, our results refine spinal cord tissue engineering strategies to optimize the regeneration of complete neurovascular bundles in their relevant spatial relationships, and further provide better understanding of axon regeneration in relation to revascularization in SCI.

Keywords: Schwann cells, scaffolds, spinal cord, axonal regeneration, revascularization, Rapamycin, stereology, Sholl analysis

1. Introduction

Traumatic spinal cord injury (SCI) occurs due to a force applied on the spine that leads to contusion, compression, partial or complete transection of the spinal cord. The primary impact results in neuronal and vascular disruption, leading to neurological impairments involving significant motor, sensory and autonomic dysfunction. The damage seen after SCI not only involves the primary insult but also a long-term secondary injury process which involves axonal loss, demyelination, inflammation, loss of structural support, cell death, increased inhibitory molecules, and glial scar formation (1). These secondary events contribute to injury severity and may also be responsible for poor regenerative potential after SCI. Unlike neurons of the peripheral nervous system (PNS), neurons in the central nervous system (CNS) have limited regenerative capacity. Apart from overcoming inhibitory factors present after injury such as glial scar formation, which acts as a physical barrier to axonal regeneration, one import factor for axonal regrowth is the availability of nutrients and oxygen, making it crucial to investigate vascularization in the regenerating spinal cord.

An effective method of investigating regeneration following SCI is through the use of multichannel scaffolds implanted into the transected spinal cord. This model allows for precise management of the local injury conditions, clear discrimination between true regeneration and remodeling or distal axonal sprouting (2-5) and reliable quantification (6). Positively-charged multichannel oligo(poly(ethylene glycol) fumarate) (OPF+) hydrogel scaffolds provide an ideal platform to control the micro-environment of the regenerating spinal cord and is amongst the most effective polymers in terms of supporting axonal regeneration (7) as it creates a micro-environment permissive for axonal regeneration (8). OPF+ was found to have enhanced neuron adherence, sustained neuron and Schwann cell viability for three weeks and promoted axon

myelination *in vitro* compared to other polymers (9). Seeding OPF+ scaffolds with Schwann cells provides guidance signals and resembles a peripheral nerve like environment, thereby promoting regeneration and myelination of axons in models of completely transected rats (10). The seven-channel design used in our investigation overlays important tracts of the rat spinal cord and enables us to independently assess and compare these structurally separated areas on each level of rat spine (as reviewed by (11)).

Axonal regeneration from neurons above and below the injury site may be impaired by physical and molecular barriers that form as a consequence of glial scarring and inflammation. Physical gaps, such as cyst formation, are commonly surrounded by areas of dense fibrosis which inhibits regeneration. Polymer scaffolds, especially when used to deliver cellular and molecular therapies, can reduce these barriers by bridging the gap. These scaffolds can resemble viable tissue with structured order and guide axonal growth through the area of the injury while creating a permissive regenerative environment by reducing scarring (8, 12). Multichannel OPF+ scaffolds can be further modified by loading them with the anti-fibrotic drug rapamycin encapsulated into poly(lactic co-glycolic acid) (PLGA) microspheres. Rapamycin is a potent immunosuppressive drug widely used to prevent allograft organ transplant rejection and has shown to reduce microglial activation, astrocyte reactivity, macrophage/neutrophil infiltration and TNF-α secretion in the SCI lesion environment (13, 14). It may also reduce fibrosis in reaction to various implanted synthetic materials (15, 16). Loading OPF+ scaffolds containing Schwann cells with rapamycin releasing microspheres was recently shown to reduce the foreign body response and promoted functional recovery after spinal cord transection in rats and demonstrated the close relationship between revascularization and axonal regeneration following spinal cord transection (17).

Promotion of new blood vessels, particularly through use of biomaterials and drugs, may confer protective and regenerative effects after injury (18, 19). Vascular disruption, ischemia and hemorrhaging occur early after SCI (20). The ruptures of blood vessels, as well as leakiness of vessels with a disrupted blood spinal cord barrier, contribute to inflammation, ultimately increasing secondary damage. The formation of an organized and functional vasculature following SCI is rare (18). However, the relationship of regenerating axons and blood vessels through biomaterials is not well understood. In addition, finding a proper combination of biomaterials, cell types, and small molecules remain to be elucidated. Our recent findings demonstrated the close relationship between blood vessel formation and the number of regenerating axons (21). We demonstrated that the formation of a capillary structure in turn supported higher numbers of regenerating axons, implicating the importance of vascular normalization in the regenerating spinal cord. In this regard, rapamycin may enhance normal vascularization of regenerating tissue and contributes to normalizing blood vessel distribution (22-25).

As the close correlation between blood vessel formation and improvement of functional recovery improvement has been well described (26-28), our objective was to assess the spatial relationships between vasculature and axons in the core area of scaffold channels six weeks after implantation of OPF+ polymer scaffolds with and without concomitant Schwann cell delivery and rapamycin administration.

2. Material and Methods

2.1 Animals

The study was approved by the Mayo Clinic Institutional Animal Care and Use Committee (IACUC). We used a total of 18 adult female Fischer rats (approximately 200 g; Harlan Laboratories, Indianapolis, USA) which were held in conventional housing on a 12 hour light-dark cycle with free access to water and chow. Care by technicians and veterinarians experienced in management of rat spinal cord injury were available daily without interruption.

2.2 Poly-lactic-co-glycolic acid (PLGA) microsphere fabrication

Drug-eluting microspheres were fabricated using a water-in-oil-in-water double emulsion and solvent evaporation technique, as we have previously described (17). Briefly, 250 mg of 50:50 D,L-poly-lactic-co-glycolic acid (PLGA) (50:50 DLG 4A, molecular weight 29 kDa, Evonik Industries AG, Essen, Germany) were dissolved in 1 ml of methylene chloride. 100 µl of a 10 mg/ml solution of rapamycin (Toronto Research Chemicals, Toronto, Canada) in absolute ethanol, or ethanol vehicle (empty microspheres) were added and emulsified by vortexing. Two ml of 2% poly(vinyl alcohol) (PVA) (Sigma-Aldrich, St. Louis, MO, USA) were added dropwise while vortexing for 30 seconds, and the resulting microsphere suspension was then poured into 100 ml of 0.3% PVA under gentle stirring on a magnetic stir plate. After one minute, 100 ml of 2% isopropyl alcohol were added and the suspension was left under gentle stirring for one hour to evaporate off the methylene chloride. The PLGA microsphere suspension was then centrifuged at 2500 RPM and washed four times with distilled water. The microspheres were placed in a -80° C freezer overnight, and freeze-dried under high vacuum.

2.3 OPF+ scaffold fabrication

Synthesis of OPF macromere was performed via condensation reaction between polyethylene glycol (PEG) and triethyamine, as previously described (29). 1g of OPF powder was dissolved in 650µl of deionized water, 0.05% (w/w) of photoinitiator (Irgacure 2959, Ciba Specialty Chemicals, Tarrytown, New York, USA) and 0.3 g of N-vinyl pyrrolidinone, a cross-linking reagent. Chemical modification with the positively charged monomer [2-(methacryloyloxy)ethyl]-trimethylammonium chloride (MAETAC) (80% wt in water; Sigma-Aldrich) followed at 20% w/w (9), producing OPF+ polymer solution. 25 mg of PLGA microspheres were added to 250 ul OPF+ liquid polymer thereafter. Scaffold fabrication was as described previously (7) via injection of the liquid polymer with suspended microspheres into a tubular glass mold containing seven parallel aligned wires as placeholders for the channel spaces. The casting was polymerized by 365 nm UV light exposure for one hour. Upon rehydration in PBS, cylindrical segments were cut to lengths of 2 mm, yielding scaffolds that were 2.6 mm in diameter and had seven longitudinal channels of 450µm diameter.

2.4 Schwann Cell (SC) isolation and culture

SCs were cultured from the sciatic nerve of 2-5 day old rat pups, as we have previously described (7). Cells were grown in SC media (DMEM/F12 medium containing 10% fetal bovine serum, 100 units/mL penicillin/streptomycin (Gibco, Grand Island, New York, USA), 2 µM forskolin (Sigma-Aldrich), and 10 ng/mL recombinant human neuregulin-1-β1 extracellular domain (R&D Systems, Minneapolis, Minnesota, USA)). SCs were initially plated onto 35-mm laminin-coated dishes and incubated at 37° C in 5% CO2 for 48 hours, and then transferred to tissue culture flasks for expansion over 4 passages before use in scaffolds.

2.5 OPF+ scaffold loading and surgical scaffold implantation

Scaffolds were sterilized by immersion in serial dilutions of ethanol (80%, 40%, 20% for 20 minutes each), followed by two washes in distilled water and incubation in SC media. OPF+ scaffolds with PLGA microspheres were loaded with SCs or Matrigel alone, as previously described (6, 10). Scaffolds were loaded with SCs resuspended in 8 ul of pre-chilled Matrigel (BD Biosciences, San Jose, California, USA) at a density of 10^5 cells/µl, whereas control animal scaffolds were loaded with Matrigel alone. Loading was performed using a gel-loading pipette tip under microscopic view at 4°C temperature, followed by three minutes at 37°C. Loaded scaffolds were incubated in SC media overnight prior to use in animal surgeries. Animal spinal cord transection surgical techniques, scaffold implantation and post-operative care were as we have previously described (8). Anesthesia was performed via intraperitoneal injection of a ketamine (80 mg/kg; Fort Dodge Animal Health, Fort Dodge, Iowa, USA) and xylazine (5 mg/kg; Lloyd Laboratories, Shenandoah, Iowa, USA). We performed a laminectomy through the T8-T10 level followed by complete T9 spinal cord transection and OPF+ scaffold implantation according to the experimental groups in the 2 mm gap between the retracted spinal cord stumps with their channels parallel to the spinal canal.

2.6 Tissue preparation and sectioning

Six weeks post-surgery, animals were sacrificed by intraperitoneal injection of 0.4 mL sodium pentobarbital (40 mg/kg) (Fort Dodge Animal Health, Fort Dodge, Iowa, USA) and transcardial perfusion with 4% paraformaldehyde in PBS was performed through the aorta. The vertebral column with spinal cord was removed en block and post fixed overnight in 4% paraformaldehyde at 4° C. The lesion site with scaffold and adjacent spinal cord ends were

dissected as 15 mm segments from the vertebral column and processed for paraffin embedding. Segments of spinal cord containing the scaffold were subsequently cut into 10 μm transverse sections on a Reichert-Jung Biocut microtome (Leica, Bannockburn, Illinois, USA) and collected on numbered slides. Tissue sections from the midpoint of the scaffold length were selected for subsequent immunohistochemistry analysis.

2.7 Antibodies and immunohistochemistry

Primary antibodies were against Tuj-1 (βIII-tubulin) for all axons (mouse anti-rat, 1:300, Millipore Chemicon, Temecula CA USA); myelin basic protein (MBP) for myelinated axons (goat anti-rat, 1:400, Santa Cruz Biotechnologies, Dallas, TX USA); and collagen IV for vessel basement membrane (rabbit anti-rat, 1:800, Abcam, Cambridge, Massachussets, USA). Secondary antibodies included Cy3-conjugated affinity purified donkey anti-mouse IgG (1:200, Millipore Chemicon) (B-III tubulin); AlexaFluor™ 647-conjugated AffiniPure donkey-anti goat IgG (1:200, Jackson ImmunoResearch Laboratories, West Grove, Pennsylvania, USA) (MBP); and Cy2-conjugated donkey anti-rabbit IgG antibody (1:200, Millipore).

Slides were deparaffinized in xylene and rehydrated by serial immersion in graded ethanol (100%, 95%, 70%) and distilled water for 5 minutes each. Antigen retrieval was performed by immersion in 1 mM EDTA in PBS, pH 8.0 in a steamer for 30 minutes (97 degrees C). Sections were washed with PBS with 0.1% Triton X-100, and blocked with 10% normal donkey serum in PBS with 0.1% Triton X-100 for 30 minutes. Primary and secondary antibodies were diluted in PBS with 5% normal donkey serum and 0.3% Triton X-100. Sections were incubated with primary antibodies at 4 degrees C overnight and secondary antibodies for 1 hour following

washing. Tissue was mounted under glass coverslips using Slow Fade Gold Antifade Reagent with DAPI nuclear stain (Molecular Probes, Eugene, Oregon, USA).

2.8 Image processing

Each individual scaffold channel was imaged using a LSM510 laser scanning confocal microscope (Carl Zeiss, Inc., Oberkochen, Germany) at 20x magnification to ensure the entire channel area was captured. A total 72 channels across the three animal groups were intact for analysis after sectioning and staining, including OPF+ scaffolds with Matrigel and empty PLGA microspheres (n=6 animals, 16 channels); OPF+ scaffold with SCs and empty PLGA microspheres (n=6 animals, 34 channels); and OPF+ scaffolds with SCs and rapamycin-eluting PLGA microspheres (n=6 animals, 22 channels). All image analysis was performed by an investigator who was blinded to the animal group using the Neurolucida software (version 11.062, MBF Bioscience, Williston, Vermont, USA).

2.8.1 Determination of core area, axons and blood vessels

Each channel contained a central, circular core of loose tissue that was histologically distinct from and circumscribed by dense, laminar tissue extending to the channel wall, as we have described (21). The core areas were manually outlined and their surface area determined by the software. Axons staining either with Tuj-1 (unmyelinated), or Tuj-1 co-localizing with MBP (myelinated) were identified and digitally marked with separate symbols (Figure 1A & 1B). The manual neuron-tracing tool was repurposed to carefully outline blood vessels along their innermost surface, and separate markers were then used to assign a number identification (Figure 1F). Vessels could be distinguished from cystic structures by the presence of a distinctive multi-layered wall containing identifiable endothelial cell nuclei, and subendothelial collagen IV

staining around an open lumen (Figure 1C). Blood vessel walls were manually outlined along their inner lumen surface, and their surface area was measured by the software. Each vessel was marked with a unique number. Only axons and vessels that were present within the outlined core boundary were marked and included in the analysis. In the process, a total of 708 blood vessel profiles, and 6667 axons (2,494 myelinated and 4,173 unmyelinated axons) were marked (Figure 2C).

2.9 Sholl analysis

Sholl analysis was used in order to assess the relationship between axon number and distance from vasculature. The core principle is to count axons falling into concentric circles, which are centered in the middle of a blood vessel. These counts can then be depicted as a function of their respective circle radii. Two values are to be predefined, namely the starting radius for the first circle and the difference in radii to each consecutive circle (Figure 2A). Neurolucida Explorer software (MBF Bioscience, Williston, Vermont, USA) was used to perform the analysis. Our starting radii were defined individually per blood vessel via manual measurement of the biggest possible diameter using the "Quick Measurement" tool. The radius of each subsequent circle was automatically determined by addition of 10µm to the previously used radius. This allowed us to adjust the analysis to individual size and form; thereby avoiding unnecessary measurement of axon counts in vessel cross-sectional area and warranting a standardized starting point in respect of vessel size and architecture for each Sholl analysis. Measured diameters ranged from 3.3 to 67.3µm. We distinguished myelinated and unmyelinated axons; an additional total count was subsequently calculated.

Axons, which were expected to be too far apart from the analyzed blood vessels to be possibly supplied by the same, were excluded after the analysis. In order to warrant a standardized procedure in doing so, we performed manual distance measurements between all blood vessels of a channel using the Quick measurement tool in Neurolucida (MBF Bioscience, Williston, Vermont, USA). The mean of all intervessel distances of a channel was then used to set a cut-off level, above which no radius and associated axon count was included in subsequent procedures. Intervessel distance means ranged from 71.36 to 236.73µm. All values were double-checked via second measurements and calculations to avoid a measurement bias and increase the validity of our numbers respectively.

The results were depicted as x/y graphs using Prism's Graph Pad (GraphPad Prism for Windows, GraphPad Software, La Jolla California USA, www.graphpad.com), whereby *axon counts* was plotted on the x and radii on the y axis. Each vessel was represented by an individual graph and all information was presented for unmyelinated, myelinated and total axon count. A Gaussian function was then fitted on every graph (Figure 2B). Each vessel's mean peak amplitude, mean peak distance and their SEMs respectively were transferred to a new table, providing information for all seven channels of an animal.

We performed the analysis for a total of 708 vessels. More detailed numbers can be found in Figure 2C above. Numbers of vessels and associated axon counts excluded after the Gaussian fit due to invalid data are presented in Figure 2D. The main reasons for exclusion were very low axon numbers and other distributions, which did not allow superimposing an accurate Gaussian curve.

2.10 Additional measurements and calculations

The mean peak density of axon number and distance was calculated as the amplitude divided by the circular area around a vessel, which was determined by the mean peak distance as radius. This parameter helped us to localize the area of highest vascular support of axonal regeneration. It was calculated manually using Microsoft Excel (2010 for Windows and 2011 for Mac). Core areas were calculated as circle area from a mean of two orthogonal diameter measurements per channel, which helped to account for differences in form. Measurements were performed using the "Quick Measurement" Tool in Neurolucida (MBF Bioscience, Williston, Vermont, USA). Calculations were performed in Microsoft Excel (2010 for Windows and 2011 for Mac). This allowed us to calculate what we called axon and vessel density. Using the core area, such as vessel and axon counts, we obtained density numbers for each reference space and channel respectively.

The marking of vessels and axons we had performed via the Neurolucida software (MBF Bioscience, Williston, Vermont, USA) allowed us to easily retrieve additional information from our samples. We obtained the cross-sectional area of each vessel via the Neurolucida Explorer software (MBF Bioscience, Williston, Vermont, USA), which calculated it from the vessel outlines.

3. Results

We have previously demonstrated that the use of OPF+ scaffolds containing rapamycin eluting microspheres were able to reduce the fibrotic reaction and improve functional motor recovery over 6 weeks (17). Here we sought to investigate the relationship of regenerating axons to the vasculature through OPF+ scaffolds containing Matrigel only (MG), Schwann cells only (SC), or Schwann cells with rapamycin (RAPA).

3.1 Relationship of core area to axon numbers and density

A distinct difference in the extent of scarring, axonal regeneration, and vessel density can be visually seen between tissue sections of the scaffold in the MG, SC, and RAPA groups (Figure 3 A-C). The channels can be thought be composed of two compartments containing an interior core of loosely regenerated axons and blood vessels surround by dense fibrotic tissue containing little or no axons/blood vessels. The axons and blood vessels in the RAPA group take up a greater area of the channel than the SC and MG groups. The mean core area of the RAPA group was larger (78,042 ± 6817 μm2) than the core areas of MG (41,829 ± 4,175 μm2) ($p=<0.0001$) or SC (51,407 μm2) ($p=0.0013$) group (Figure 3D). Although the core area between the MG and SC groups were not different, there was a trend towards the SC group having a greater core area and less scarring ($p=0.085$).

Even though the RAPA group had a larger core, the axons appear scattered whereas in the SC group there are many clusters containing both myelinated and unmyelinated axons (Figure 3). The SC group (147.5 ± 17.03 axons/channel) had a significantly greater mean number of axons per channel than the MG (41.78 ± 8.35 axons/channel; $p=<0.0001$) or RAPA groups (43.23 ± 7.2 axons/channel; $p=<0.0001$; Figure 2C & 4A). This relationship held true when the unmyelinated

and myelinated axons were counted separately, the SC group had many more myelinated and unmyelinated axons per channel than the MG or RAPA groups (Figure 2C and 4A). The axon density was explored (number of axons/core area), the same relationship was found where axon density of the SC group (0.003 ± 0.00039 axons/μm2) was greater than that of the MG (0.00114 ± 0.00023 axons/μm2; p=<0.0001) or RAPA groups (0.0006 ± 0.0001 axons/μm2; p=<0.0001; Figure 3E). When the myelinated and unmyelinated axons were separately analyzed, again the SC group had superior numbers to the MG and RAPA groups.

3.2 Relationship of core area to blood vessel numbers and density

In histological samples (Figure 3C), it is observable that the RAPA group had smaller vessels but not necessarily less. The mean surface area occupied by vessels in the SC group (1,529 ± 286.2 μm2) was significantly higher than of the vessel area in MG (666 ± 164.9 μm2; p=0.0307) and RAPA (538.8 ± 120.5 μm2; p=0.01). There was no significant differences between the number of vessels between the RAPA group (10.41 ± 0.95 vessels) when compare to the MG (8.313 ± 0.78 vessels) and SC (10.18 ± 0.62 vessels) groups (Figure 4B). However, there was a negative correlation between vessel density and core area in all three groups (MG: Spearman r=-0.5795, p=0.0186; SC: Spearman r=-0.5129, p=0.0019; RAPA: Spearman r=-0.4884, p=0.0211; Figure 3F). As it could be predicted, the mean intervessel distribution in the RAPA group (146.1 ± 8.65 μm) was increased when compared to MG (96.94 ± 5.66 μm; p=<0.0001) and SC (116.5 ± 3.947 μm; p=0.0013; Figure 4F) groups.

Unbiased stereology was used to make volumetric measurements of vessel volume, number, surface area, cross sectional area, diameter, and radial diffusion distance. SC group had large vessel volume (16,528 ± 3088 μm3) than MG (7745 ± 147 6 μm3; p=0.0553) and RAPA (8318 ±

1990 μm3; p=0.0607; Figure 4C) groups. The total vessel length was not significantly different between the groups (Figure 4D). The total vessel surface area was greater in the SC group (3150 ± 386.1 μm2) than in the MG (1878 ± 334.5 μm2; p=0.0612) or RAPA (2070 ± 322 μm2; p=0.0999) group, although this comparison was not significant (Figure 4E). The mean cross sectional area of the vessels also trended towards being greater in the SC group (2655 ± 1178 μm2) than the MG (177.2±71.52μm2) or RAPA (1376±1151μm2) groups but was not significant (Figure 4H). The mean vessel diameter was found to be not significantly different between the groups (Figure 4I), although the RAPA (4.14 ± 1.56 μm) and SC (4.93 ± 0.94 μm) group values were approximately twice as large as the MG group (2.44 ± 0.47 μm). Radial diffusion distances were derived from the diameter values and amounted to 23.68 ± 1.81 μm in the MG, 28.34 ± 3.52 μm in the SC and 34.37 μm in the RAPA group, which were not statistically different between groups.

3.3 Relationship of regenerating axons to blood vessels in the scaffold channels

For each blood vessel, the mean peak distribution amplitude and distance (Figure 5) were plotted as a function of the respective vessel cross-sectional areas. Greater number of axons was found in the SC group (Figure 5B and 5E) and fewer myelinated axons were found in the RAPA group (Figure 5C and 5F). Overall, this analysis demonstrated that smaller vessels support high axon numbers in all the groups.

Plotting mean peak distance versus mean peak amplitude (Figure 6) showed a minimum distance of approximately 25 μm for the highest axon concentration to the respective vessel. This effect could be observed throughout all groups and regardless of looking at myelinated, unmyelinated or total axon count. The effect was slightly less pronounced in the RAPA group. Peak axonal

density describes the density of the highest concentration of axons in respect to a circular area, determined by the mean peak distance as radius and the vessel center as center point. Plotting these values against vessel cross-sectional area allowed for a correlation analysis between vascular caliber and support of axonal regeneration (Figure 6C, 6F, and 6I). We found a significant negative correlation (Spearman r=-0.1431, p=0.0257) between peaked axonal density and vessel cross-sectional area analyzing the total axon count of the SC group (Figure 6I). This demonstrates that smaller vessels support more axons.

3.4 Distribution and relationship of regenerating axons to each other

Cumulative distribution functions (CDFs) of inter-axon distances were generated using a statistical spatial algorithm within each scaffold channel type (Figure 7). Axons can be distributed as random, clustered, or dispersed points in space (Figure 7A). The closest neighbor analysis (G-Function; Figure 7B) demonstrated that 90% of axons in the MG or SC groups were located under 10 μm from the next closest axon (Figure 7D and 7E). The RAPA group (Figure 6F) was more dispersed with 90% of the axons 16 μm from the next closest axon. Analysis of the distance of an axon to an arbitrary point in space (F-function) showed that axons were distributed in a clustered distribution (Figure 7G-H), regardless of the condition, since the distance between axons and random points was smaller than random points alone.

4. Discussion

In this study, we demonstrate methods by which axonal regeneration and revascularization can be quantified. Most of our presented measurements and results are novel in this field, leaving us with very few other examples and comparable outcomes in the literature. However, the stereological estimations and the derived calculations used in this study are well established (30) and stereological quantification of vascular beds of the brain and spinal cord has been described extensively (31). We have established a relationship between vascular- and growth-supportive properties of SCs delivered to the injury site via polymer scaffolds with and without concomitant administration of rapamycin. In doing so, this study focuses on the influence of rapamycin on the extent of scarring and ultimately how scarring of the scaffold can affect axonal and vessel distribution. This study identifies the vascular – axonal relationship through extensive measurements, distribution analyses and stereology of the injury site and described novel techniques to analyze their interactions after spinal cord injury in three different groups (MG, SCs, and RAPA). There was a significant negative correlation between peaked axonal density and vessel-cross sectional area, confirming that a small radial diffusion distance is a necessity for successful axonal regeneration; supporting previous observations that blood flow rate plays a major role in axonal regeneration (21).

Scaffolds loaded with rapamycin- releasing microspheres were previously found to promote peripheral nerve regeneration when implanted in the early phase of sciatic nerve injury (32). Our lab has previously demonstrated that administration of rapamycin resulted in improved functional recovery following spinal cord transection, which was linked to improved axonal regeneration, possibly through increased BDNF and GDNF secretion of transplanted SCs (17). Although rapamycin was found to promote secretion of nerve growth factors, and has been

suggested for application in peripheral nerve regeneration therapy (33, 34), our study found a significantly greater number of myelinated and unmyelinated axons per channel in the SC group, which were more clustered compared to the MG and RAPA group. This observation makes sense since rapamycin is an allosteric mTOR inhibitor and mTOR activity has been shown to aid axonal regeneration following CNS and PNS injuries (35). The results presented here indicate that improved motor function recovery does not solely depend on higher axon numbers or axon density, but may also be associated with reduced fibrosis and inflammation. The use of rapamycin after N-methyl-D-aspartate induced retinal injury showed a decrease in CD45 positive cells and Iba1 positive cells while having reduced vascular damage (36). In addition, rapamycin treatment in SCI rats demonstrated to decrease tumor necrosis factor production, reduced the number of activated microglia, and promoted autophagy resulting in functional improvements (17, 37). Fibrotic scar formation in the lesion site is also considered to be an obstacle to axonal regeneration and suppressing this process has been suggested as a reliable strategy to promote regeneration (38). Rapamycin has been found to inhibit proliferation of fibroblasts, stimulate their apoptosis and decrease collagen synthesis (39). In correlation with this, we observed a larger mean core area in the RAPA group, indicating reduced scarring in this group. These results indicate that while there may not be an increased number of axons, there may be other routes through which functional benefit can be conferred.

Rapamycin administration resulted in smaller vessels, however, without affecting vessel density compared to the other groups. Few studies have investigated the effects of rapamycin on vascularization following spinal cord injury; however, there is also substantial evidence for its anti-angiogenic and growth-inhibitory properties in the nervous system (40-42) , which may be dose dependent. To our knowledge, this study is the first to provide extensive volumetric

measurements to study the effects of rapamycin on vessel volume, number, surface area, cross sectional area, diameter and radial diffusion distance. There was a significant negative correlation between peaked axonal density and vessel-cross-sectional area in the SC group and similar trends in the other animal groups, indicating that smaller vessels support more axons. Micro-vessels in the CNS are known to provide tremendous trophic support (43) as well as be critical for tissue survival (44, 45). Furthermore, regenerating axons have been shown to grow along blood vessels (46). Methods that limit vascular damage, improve vessel density, and restore blood flow to the injured cord may provide a foundation for spinal cord repair and recovery (47, 48). A number of other studies reported that increases in blood vessel density correlate with improvements in recovery after spinal cord injury (26-28). Even though we could not directly show a significant correlation between axon counts and radial diffusion distances in the treatment groups, we were able to observe a trend towards higher radial diffusion distances in the SC group and significantly higher axon counts compared to the MG-only group. Our stereological estimates found significantly larger inter-vessel distances combined with higher radial diffusion distances which were associated with decreased axon counts in the RAPA group. We previously reported that radial diffusion distances in vessels significantly correlate to axon numbers, demonstrating the need to engineer higher numbers of small vessels in parallel to improve axonal density (21). This finding should be considered with regard to the relative equality in total vessel counts throughout the groups and the larger core area. Larger core areas may negatively affect the blood supply in RAPA loaded scaffolds, as vasculature must support a larger area which in turn could play a role in the reduced axon counts.

The distribution of axons and blood vessels plays an important role in development. When neuropilin 1 (NRP1) is knocked out of endothelial cells in a mouse model, there was abnormal

formation of vessels in the optic nerve which lead to abnormal axon distribution (49). Normally the vessels line the outside of the axon bundle, however with this mutation the vessels are seen penetrating the axon bundles leading to exclusion zones where abnormal holes are found in the optic nerve. In addition, the vessel diameter was found to be larger in the *Nrp1*$^{fl/-}$*;Tie2-Cre* mutants, suggesting that smaller blood vessels facilitate passive co-existence with axons. These findings match with our findings in the spinal cord that smaller diameter vessels and close axon bundles were associated with higher axon counts, suggesting that the interplay between vessel size and distance can greatly influence axon distribution and regeneration. In attempting to promote regeneration, there is a balance between vessels being able to remove waste and provide growth factors without obstructing axon growth.

Using cumulative distribution functions (CDFs) we were able to identify a clustered appearance of axons in the SC and partly MG group, whereas axons in the RAPA group usually seemed to be localized alone in a dispersed distribution. RAPA prevents the formation of a fibrotic scar that may lead to a more dispersed distribution but there was no contribution to axon number. The closest neighbor axon in the RAPA group was 16 um, whereas in the other conditions they were 10 um apart. Axon proximity may be an important but understudied aspect in neuroregeneration. In development, axons connecting from the retina to the lateral geniculate nucleus (LGN) follow not only chemical but electrical cues (50). Meister *et al*. (1991) demonstrated that axons that are the nearest to each other are electrically active at the same time and this simultaneous activity can influence the environment to help navigate to the target together. Furthermore, blocking electrical activity with tetrodotoxin in the LGN during development leads to abnormal patterning of connections to the visual cortex, highlighting the importance of electrical signaling between neighboring neurons (51). The closer proximity and greater number of axons could aid in

pathfinding of spinal axons in OPF scaffolds as well. However, we have previously demonstrated that the use of rapamycin containing scaffolds loaded with Schwann cells resulted in better functional recovery following SCI, demonstrating the increased axonal number is not the only factor in functional recovery but reduction in inflammation and scarring can contribute through other mechanisms.

5. Conclusion

Angiogenesis plays a major role in axonal regeneration following SCI and we have developed novel methods to investigate axon-vessel relationships. Our study found differences in axonal regeneration, scarring and vessel density, which were measured and visually detected between the three scaffold groups (MG, SC and RAPA). Our measurements provide highly relevant methods to further study the regenerative environment after SCI and will help future investigations in this field.

Acknowledgments:

This work was generously funded by grants from the National Institute of Biomedical Imagining and Bioengineering (EB02390), National Institute of Biomedical Imagining and Bioengineering (TL1 TR002380), Morton Cure Paralysis Fund, and Craig H. Nielsen Foundation. The author would like to acknowledge the technical assistance of Jarred Nesbitt and administrative assistance of Jane Meyer.

Conflict of Interest:

No conflict of interests.

References:

1. Siddiqui, A.M., Khazaei, M., andFehlings, M.G. Translating mechanisms of neuroprotection, regeneration, and repair to treatment of spinal cord injury. Progress in brain research: Elsevier; 2015. pp. 15.

2. Friedman, J.A., Moore, M.J., Yaszemski, M.J., Lewellyn, E., Spinner, R.J., Currier, B.L., andWindebank, A.J. Biodegradable polymer implants to promote axonal regeneration following spinal cord injury. Program No 2032 2002 Abstract Viewer/Itinerary Planner Washington, DC: Society for Neuroscience Online 2002.

3. Xu, X.M., Zhang, S.X., Li, H., Aebischer, P., andBunge, M.B. Regrowth of axons into the distal spinal cord through a Schwann-cell-seeded mini-channel implanted into hemisected adult rat spinal cord. Eur J Neurosci **11**, 1723, 1999.

4. Oudega, M., andXu, X.M. Schwann cell transplantation for repair of the adult spinal cord. J Neurotrauma **23**, 453, 2006.

5. Teng, Y.D., Lavik, E.B., Qu, X., Park, K.I., Ourednik, J., Zurakowski, D., Langer, R., andSnyder, E.Y. Functional recovery following traumatic spinal cord injury mediated by a unique polymer scaffold seeded with neural stem cells. Proceedings of the National Academy of Sciences **99**, 3024, 2002.

6. Olson, H.E., Rooney, G.E., Gross, L., Nesbitt, J.J., Galvin, K.E., Knight, A., Chen, B., Yaszemski, M.J., andWindebank, A.J. Neural stem cell- and schwann cell-loaded biodegradable polymer scaffolds support axonal regeneration in the transected spinal cord. Tissue Eng Part A **15**, 1797, 2009.

7. Chen, B.K., Knight, A.M., Madigan, N.N., Gross, L., Dadsetan, M., Nesbitt, J.J., Rooney, G.E., Currier, B.L., Yaszemski, M.J., Spinner, R.J., andWindebank, A.J. Comparison of polymer

scaffolds in rat spinal cord: A step toward quantitative assessment of combinatorial approaches to spinal cord repair. Biomaterials **32**, 8077, 2011.

8. Hakim, J.S., Esmaeili Rad, M., Grahn, P.J., Chen, B.K., Knight, A.M., Schmeichel, A.M., Isaq, N.A., Dadsetan, M., Yaszemski, M.J., andWindebank, A.J. Positively Charged Oligo[Poly(Ethylene Glycol) Fumarate] Scaffold Implantation Results in a Permissive Lesion Environment after Spinal Cord Injury in Rat. Tissue Eng Part A **21**, 2099, 2015.

9. Dadsetan, M., Knight, A.M., Lu, L., Windebank, A.J., andYaszemski, M.J. Stimulation of neurite outgrowth using positively charged hydrogels. Biomaterials **30**, 3874, 2009.

10. Chen, B.K., Knight, A.M., de Ruiter, G.C.W., Yaszemski, M.J., Currier, B.L., andWindebank, A.J. Axon regeneration through scaffold into distal spinal cord after transection. J Neurotrauma **26**, 1759, 2009.

11. Madigan, N.N., McMahon, S., O'Brien, T., Yaszemski, M.J., andWindebank, A.J. Current tissue engineering and novel therapeutic approaches to axonal regeneration following spinal cord injury using polymer scaffolds. Respir Physiol Neurobiol **169**, 183, 2009.

12. Madigan, N.N., Rooney, G., Knight, A., Chen, B., Gross, L., Dadsetan, M., Nesbitt, J., Yaszemski, M., McMahon, S., andWindebank, A. Axonal regeneration supported by neurotrophic Schwann cells and mesenchymal stem cells through polymer scaffolds in the transected rat spinal cord. Society for Neuroscience, Program No 3652/CC71, Chicago, IL 2009.

13. Goldshmit, Y., Kanner, S., Zacs, M., Frisca, F., Pinto, A.R., Currie, P.D., andPinkas-Kramarski, R. Rapamycin increases neuronal survival, reduces inflammation and astrocyte proliferation after spinal cord injury. Mol Cell Neurosci **68**, 82, 2015.

14. Tateda, S., Kanno, H., Ozawa, H., Sekiguchi, A., Yahata, K., Yamaya, S., andItoi, E. Rapamycin suppresses microglial activation and reduces the development of neuropathic pain after spinal cord injury. J Orthop Res **35**, 93, 2017.

15. Morice, M.C., Serruys, P.W., Sousa, J.E., Fajadet, J., Ban Hayashi, E., Perin, M., Colombo, A., Schuler, G., Barragan, P., Guagliumi, G., Molnar, F., andFalotico, R. A randomized comparison of a sirolimus-eluting stent with a standard stent for coronary revascularization. N Engl J Med **346**, 1773, 2002.

16. Moses, J.W., Leon, M.B., Popma, J.J., Fitzgerald, P.J., Holmes, D.R., O'Shaughnessy, C., Caputo, R.P., Kereiakes, D.J., Williams, D.O., Teirstein, P.S., Jaeger, J.L., andKuntz, R.E. Sirolimus-eluting stents versus standard stents in patients with stenosis in a native coronary artery. N Engl J Med **349**, 1315, 2003.

17. Hakim, J.S., Rodysill, B.R., Chen, B.K., Schmeichel, A.M., Yaszemski, M.J., Windebank, A.J., andMadigan, N.N. Combinatorial Tissue Engineering Partially Restores Function after Spinal Cord Injury. Journal of tissue engineering and regenerative medicine 2019.

18. Haggerty, A.E., Maldonado-Lasunción, I., andOudega, M. Biomaterials for revascularization and immunomodulation after spinal cord injury. Biomedical Materials **13**, 044105, 2018.

19. Siddiqui, A.M., Ahuja, C.S., Tator, C.H., andFehlings, M.G. Chapter 3: Spinal cord protective and regenerative therapies. In: Jallo J., Vaccaro A., eds. Neurotrauma and Critical Care of the Spine; Second Edition. Second ed: Thieme; 2018. pp. 238.

20. Tator, C.H., andFehlings, M.G. Review of the secondary injury theory of acute spinal cord trauma with emphasis on vascular mechanisms. Journal of neurosurgery **75**, 15, 1991.

21. Madigan, N.N., Chen, B.K., Knight, A.M., Rooney, G.E., Sweeney, E., Kinnavane, L., Yaszemski, M.J., Dockery, P., O'Brien, T., McMahon, S.S., andWindebank, A.J. Comparison of

Cellular Architecture, Axonal Growth, and Blood Vessel Formation Through Cell-Loaded Polymer Scaffolds in the Transected Rat Spinal Cord. Tissue Eng Part A **20**, 2985, 2014.

22. Guba, M., von Breitenbuch, P., Steinbauer, M., Koehl, G., Flegel, S., Hornung, M., Bruns, C.J., Zuelke, C., Farkas, S., Anthuber, M., Jauch, K.W., andGeissler, E.K. Rapamycin inhibits primary and metastatic tumor growth by antiangiogenesis: involvement of vascular endothelial growth factor. Nat Med **8**, 128, 2002.

23. Jain, R.K. Normalizing tumor vasculature with anti-angiogenic therapy: a new paradigm for combination therapy. Nat Med **7**, 987, 2001.

24. Jain, R.K. Normalization of tumor vasculature: an emerging concept in antiangiogenic therapy. Science **307**, 58, 2005.

25. Gao, K., Wang, Y.S., Yuan, Y.J., Wan, Z.H., Yao, T.C., Li, H.H., Tang, P.F., andMei, X.F. Neuroprotective effect of rapamycin on spinal cord injury via activation of the Wnt/beta-catenin signaling pathway. Neural Regen Res **10**, 951, 2015.

26. Glaser, J., Gonzalez, R., Sadr, E., andKeirstead, H.S. Neutralization of the chemokine CXCL10 reduces apoptosis and increases axon sprouting after spinal cord injury. Journal of neuroscience research **84**, 724, 2006.

27. Kaneko, S., Iwanami, A., Nakamura, M., Kishino, A., Kikuchi, K., Shibata, S., Okano, H.J., Ikegami, T., Moriya, A., andKonishi, O. A selective Sema3A inhibitor enhances regenerative responses and functional recovery of the injured spinal cord. Nature medicine **12**, 1380, 2006.

28. Yoshihara, T., Ohta, M., Itokazu, Y., Matsumoto, N., Dezawa, M., Suzuki, Y., Taguchi, A., Watanabe, Y., Adachi, Y., andIkehara, S. Neuroprotective effect of bone marrow–derived mononuclear cells promoting functional recovery from spinal cord injury. Journal of Neurotrauma **24**, 1026, 2007.

29. Dadsetan, M., Szatkowski, J.P., Yaszemski, M.J., andLu, L. Characterization of photo-cross-linked oligo[poly(ethylene glycol) fumarate] hydrogels for cartilage tissue engineering. Biomacromolecules **8**, 1702, 2007.

30. Howard, V., andReed, M. Unbiased stereology: three-dimensional measurement in microscopy: Garland Science; 2004.

31. Dockery, P., andFraher, J. The quantification of vascular beds: a stereological approach. Experimental and molecular pathology **82**, 110, 2007.

32. Si, H.B., Zeng, Y., Lu, Y.R., Cheng, J.Q., andShen, B. Control-released basic fibroblast growth factor-loaded poly-lactic-co-glycolic acid microspheres promote sciatic nerve regeneration in rats. Experimental and therapeutic medicine **13**, 429, 2017.

33. Ding, T., Zhu, C., Yin, J.-B., Zhang, T., Lu, Y.-C., Ren, J., andLi, Y.-Q. Slow-releasing rapamycin-coated bionic peripheral nerve scaffold promotes the regeneration of rat sciatic nerve after injury. Life sciences **122**, 92, 2015.

34. Liu, F., Zhang, H., Zhang, K., Wang, X., Li, S., andYin, Y. Rapamycin promotes Schwann cell migration and nerve growth factor secretion. Neural regeneration research **9**, 602, 2014.

35. Abe, N., Borson, S.H., Gambello, M.J., Wang, F., andCavalli, V. Mammalian target of rapamycin (mTOR) activation increases axonal growth capacity of injured peripheral nerves. Journal of Biological Chemistry **285**, 28034, 2010.

36. Aoki, Y., Nakahara, T., Asano, D., Ushikubo, H., Mori, A., Sakamoto, K., andIshii, K. Preventive effects of rapamycin on inflammation and capillary degeneration in a rat model of NMDA-induced retinal injury. Biological and Pharmaceutical Bulletin **38**, 321, 2015.

37. Chen, H.-C., Fong, T.-H., Hsu, P.-W., andChiu, W.-T. Multifaceted effects of rapamycin on functional recovery after spinal cord injury in rats through autophagy promotion, anti-inflammation, and neuroprotection. journal of surgical research **179**, e203, 2013.

38. Yoshioka, N., Hisanaga, S.I., andKawano, H. Suppression of fibrotic scar formation promotes axonal regeneration without disturbing blood-brain barrier repair and withdrawal of leukocytes after traumatic brain injury. Journal of Comparative Neurology **518**, 3867, 2010.

39. Sun, Y., Zhao, S., Li, X., Yan, L., Wang, J., Wang, D., Chen, H., Dai, J., andHe, J. Local application of rapamycin reduces epidural fibrosis after laminectomy via inhibiting fibroblast proliferation and prompting apoptosis. Journal of orthopaedic surgery and research **11**, 58, 2016.

40. Guba, M., von Breitenbuch, P., Steinbauer, M., Koehl, G., Flegel, S., Hornung, M., Bruns, C.J., Zuelke, C., Farkas, S., andAnthuber, M. Rapamycin inhibits primary and metastatic tumor growth by antiangiogenesis: involvement of vascular endothelial growth factor. Nature medicine **8**, 128, 2002.

41. Dejneka, N.S., Kuroki, A.M., Fosnot, J., Tang, W., Tolentino, M.J., andBennett, J. Systemic rapamycin inhibits retinal and choroidal neovascularization in mice. Mol Vis **10**, 964, 2004.

42. Yagasaki, R., Nakahara, T., Ushikubo, H., Mori, A., Sakamoto, K., andIshii, K. Anti-angiogenic effects of mammalian target of rapamycin inhibitors in a mouse model of oxygen-induced retinopathy. Biological and Pharmaceutical Bulletin **37**, 1838, 2014.

43. Raab, S., andPlate, K.H. Different networks, common growth factors: shared growth factors and receptors of the vascular and the nervous system. Acta neuropathologica **113**, 607, 2007.

44. Richardson, T.P., Peters, M.C., Ennett, A.B., andMooney, D.J. Polymeric system for dual growth factor delivery. Nature biotechnology **19**, 1029, 2001.

45. Peters, M.C., Polverini, P.J., andMooney, D.J. Engineering vascular networks in porous polymer matrices. Journal of Biomedical Materials Research: An Official Journal of The Society for Biomaterials, The Japanese Society for Biomaterials, and The Australian Society for Biomaterials and the Korean Society for Biomaterials **60**, 668, 2002.

46. Bearden, S.E., andSegal, S.S. Neurovascular alignment in adult mouse skeletal muscles. Microcirculation **12**, 161, 2005.

47. Ng, M.T., Stammers, A.T., andKwon, B.K. Vascular disruption and the role of angiogenic proteins after spinal cord injury. Translational stroke research **2**, 474, 2011.

48. Furlan, J.C., andFehlings, M.G. Cardiovascular complications after acute spinal cord injury: pathophysiology, diagnosis, and management. Neurosurgical focus **25**, E13, 2008.

49. Erskine, L., François, U., Denti, L., Joyce, A., Tillo, M., Bruce, F., Vargesson, N., andRuhrberg, C. VEGF-A and neuropilin 1 (NRP1) shape axon projections in the developing CNS via dual roles in neurons and blood vessels. Development **144**, 2504, 2017.

50. Meister, M., Wong, R., Baylor, D., andShatz, C. Synchronous bursts of action potentials in ganglion cells of the developing mammalian retina. Science **252**, 939, 1991.

51. Catalano, S.M., and Shatz, C.J. Activity-Dependent Cortical Target Selection by Thalamic Axons. Science **281**, 559, 1998.

1 **Figures:**

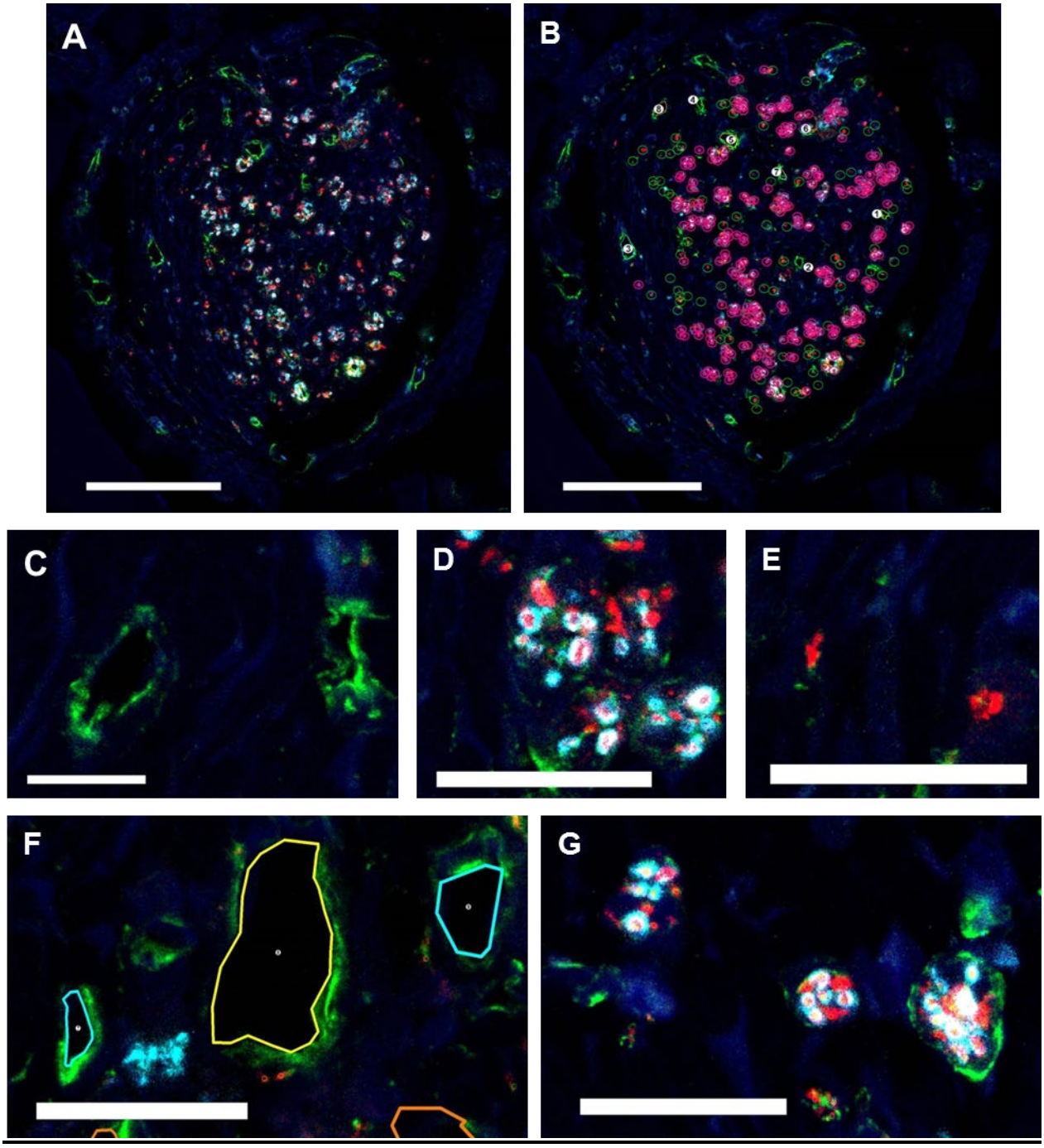

2

3

4

5

Figure 1: Image processing using Neurolucida software to mark and measure vessels, myelinated axons, and unmyelinated axons through an OPF+ scaffold. (A) Example of a confocal image of a channel in the OPF+ scaffold following spinal cord implantation before marking and **(B)** after marking. DAPI (blue), neuron were labelled with β-tubulin (red), myelin basic protein is used to label the myelin (cyan), and collagen IV was used to mark the blood vessels (green). Scale bar = 100 µm. **(C)** Example of 2 blood vessels before marking. Collagen IV (green) surrounds an empty vessel lumen. **(D)** Myelinated axons and unmyelinated axons can be determine by the presences of a myelin basic protein 'halo' (cyan) around a punctate axon containing β-tubulin (red). **(E)** Unmyelinated axons. **(F)** Marked and outlined blood vessels. (G) Marked myelinated and unmyelinated axons. Scale bar = 30 µm.

A

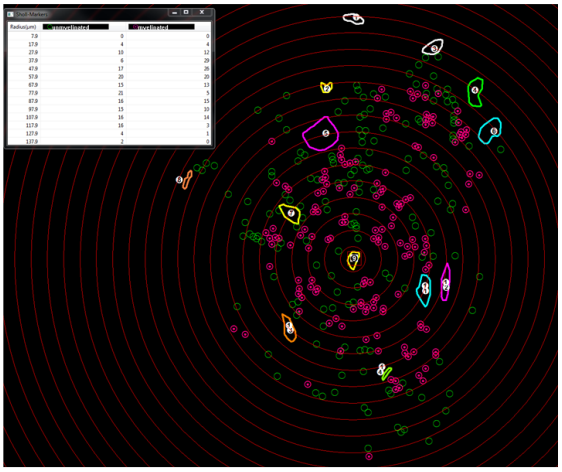

B

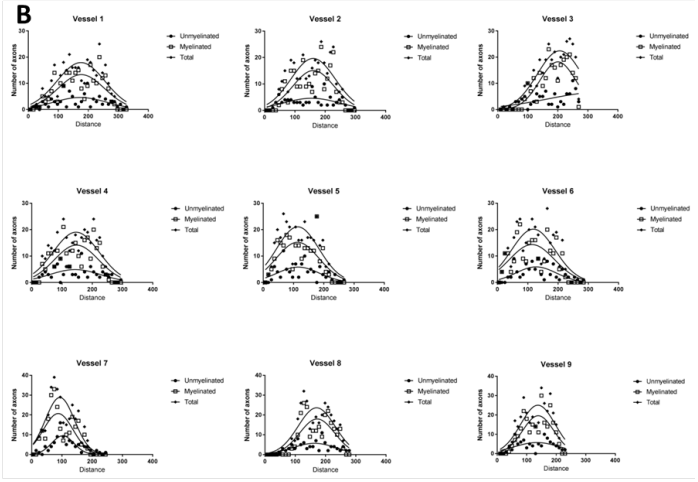

C

Marked structure:	Vessels	um Axons	m Axons	Total Axons
MG	133	495	207	702
SC	346	2796	2218	5014
RAPA	229	882	69	951
Total	708	4173	2494	6667

[Number of channels: 16 Matrigel; 34 SC; 22 SC + Rapamycin.]

D

excluded values	entire vessels	um	m	total
MG	55	68/13	105/50	59/4
SC	71	105/50	166/95	98/27
RAPA	65	74/11	225/160	82/17

1

2

3

4

5

6

7

8

9

Figure 2: Sholl analysis was conducted and Gaussian function was fitted to the data to determine the relationship between axon number and distance from vasculature. (A) Measurement of axon distribution was done using concentric circles (10 μm apart) with the vessel being analyzed in the center. Results are depicted as circle radius for unmyelinated (open circles) and myelinated axons (encircled points). **(B)** The number of axons within each 10 micron radial increment was then plotted as a function of the distance for each blood vessel, and consistently demonstrated a Gaussian distribution. This data can be compressed by using mean peak amplitude to sample axon number and mean peak distance to sample axonal distances from the vessel. **(C)** Markings in each OPF+ scaffold channel for unmyelinated, myelinated axons, and blood vessels in each animal group were measured as cumulative counts. **(D)** The number of axons and vessels excluded after Gaussian fit due to invalid data such as low axon numbers.

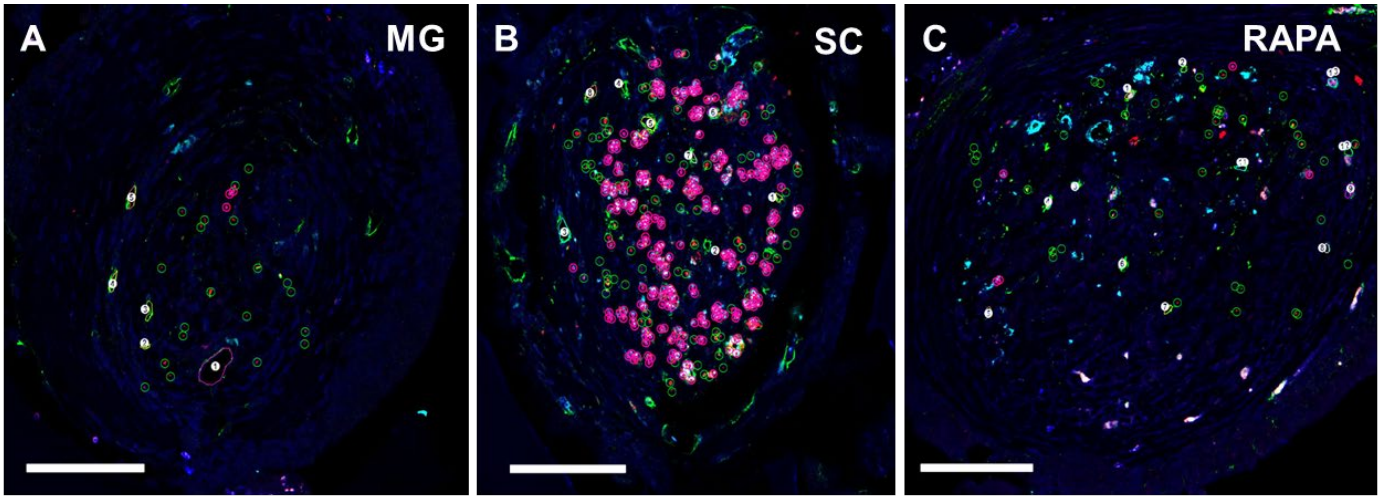

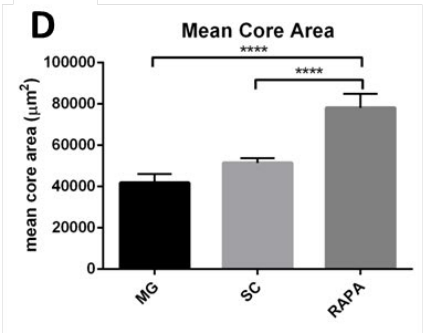

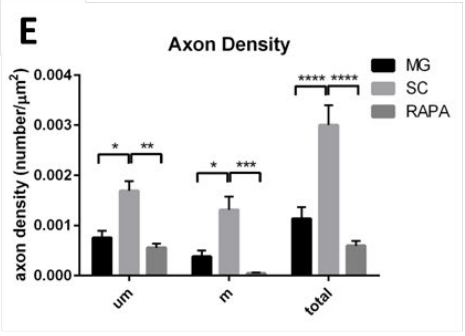

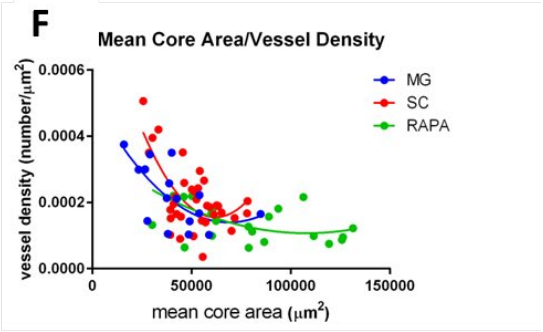

1

2

3

4

5

6

7

8

9

Figure 3: Axon and blood vessel density in relationship to core area. The core area, axon number, and blood vessel numbers were determined using Neurolucida software for rats implanted with OPF+ scaffold channels containing **(A)** matrigel only (MG), **(B)** Schwann cells (SC), or **(C)** Schwann cells with rapamycin microspheres (RAPA). Scale bar = 100 µm. **(D)** Rats in the RAPA group had a larger mean core area than those in the SC or MG groups. **(E)** SC group had greater axon densities in all categories (um=unmyelinated, m=myelinated) when compared to RAPA and MG groups. **(F)** There was a negative correlation between mean core are and vessel density for all groups.

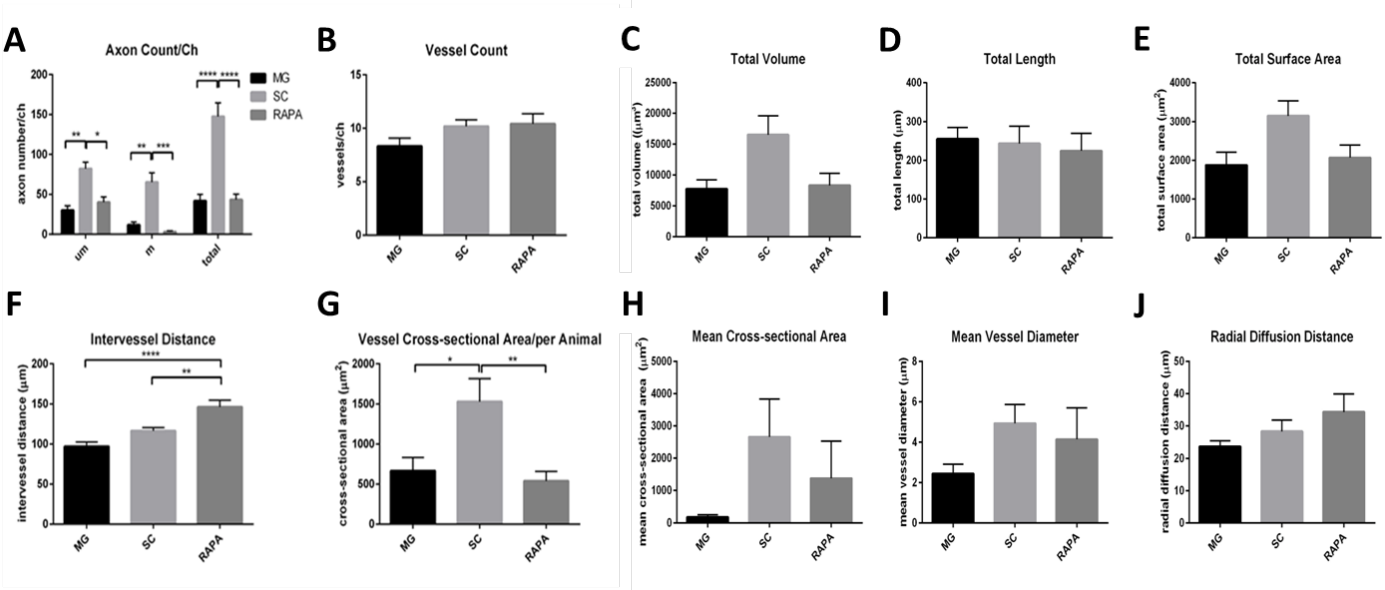

Figure 4: Axon counts, vessel counts, and other vessel characteristics determined by stereological analysis of scaffolds implanted in the transected spinal cord. (A) Mean axon counts per scaffold channel. Schwann cell loaded channels (SC) supported more myelinated and unmyelinated axonal regeneration than Matrigel (MG) or Schwann cell scaffolds eluting rapamycin (RAPA). **(B)**. Mean amount of blood vessels per scaffold channel. **(C)** Serological estimates were made to determine blood vessel volume, **(D)** length, and **(E)** surface area. **(F)** Blood vessels were further characterized by their intervessel distances, and **(G)** mean cross-sectional area in each group. **(H)** Stereological estimates were also made to determine the mean cross sectional area of the blood vessels, **(I)** means blood vessel diameter, and the **(J)** radial diffusion area. Stereology helped determine that the number of vessels was the same in each group, vessels were larger in Schwann cell only animals, and the distances between vessels was greater with rapamycin treatment.

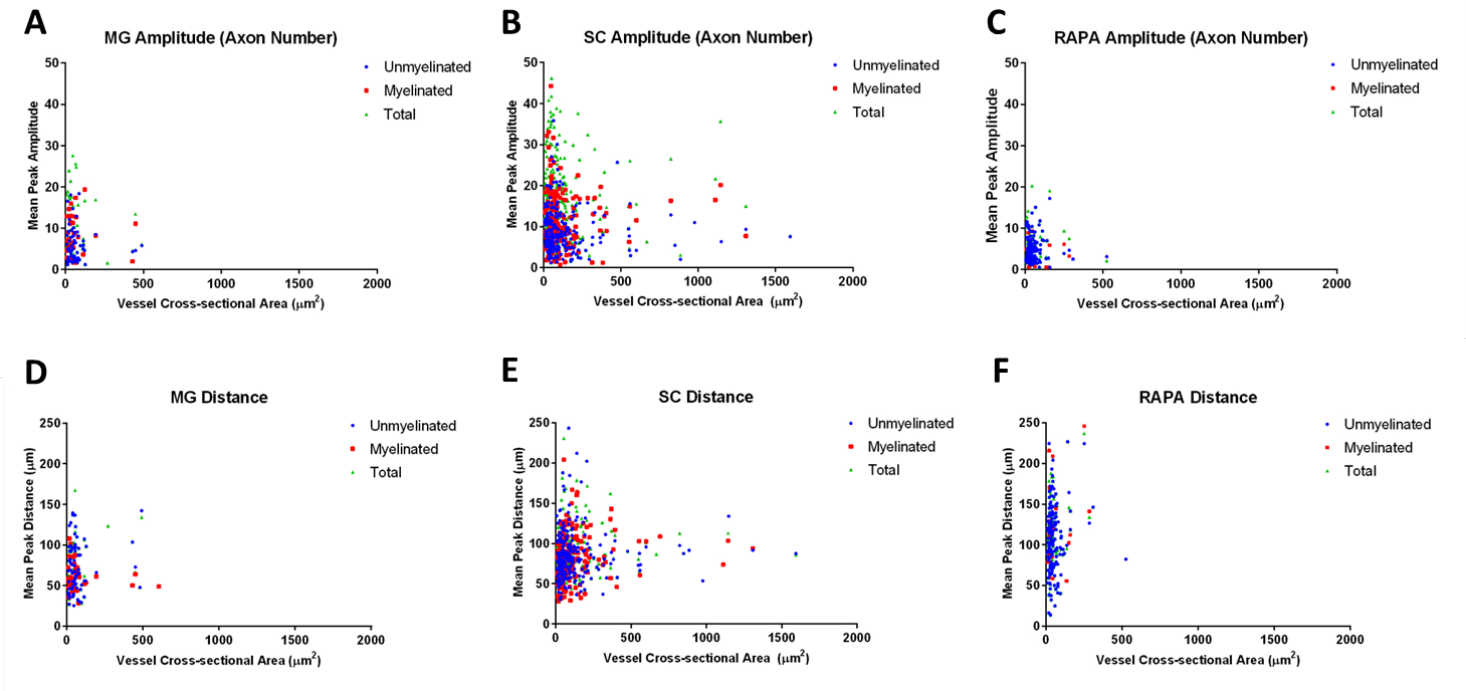

1

2

3

4

5

6

7

8

9

10

Figure 5: Mean peak amplitude and mean peak distance of axons compared to blood vessel cross sectional area. Unmyelinated, myelinated, and total axon counts were represented by individual graphs for each vessel. The graph was fitted to a Gaussian function and then the **(A-C)** mean peak amplitude and **(D-F)** mean peak distance was calculated for rats treated with OPF+ scaffolds containing Matrigel (MG), Schwann cells (SC), or Schwann cells with rapamycin microspheres (RAPA).

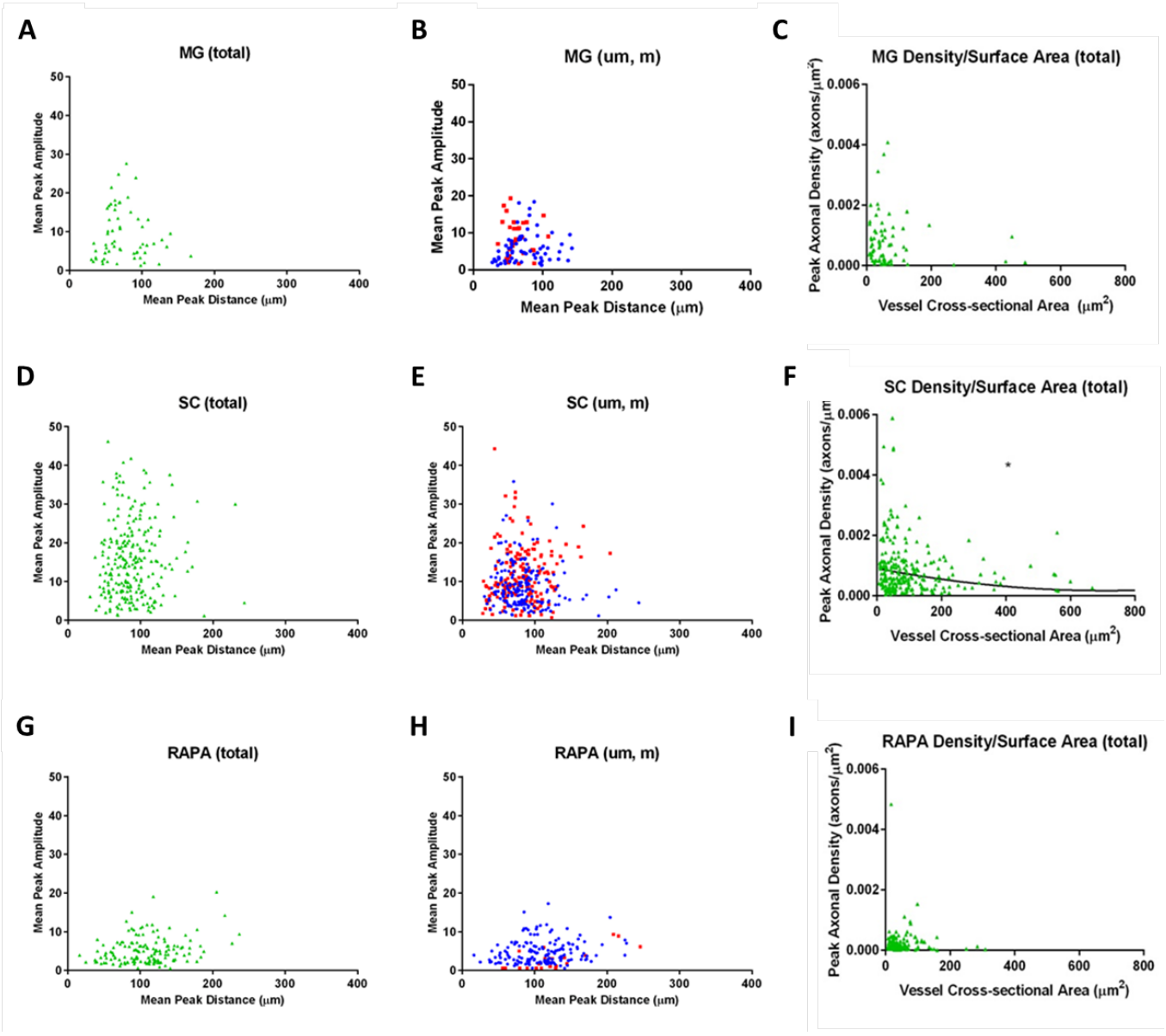

Figure 6: Spatial relationship of axons to blood vessels. (A, B, D, E, G, H) Mean peak amplitude versus mean peak distance. (left: total axon count, right: unmyelinated and myelinated axon count; blue circles=unmyelinated red squares=myelinated. Pattern of the Gaussian distribution of axons distance and density around blood vessels was measured. The distribution was concentrated within concentric distance of 200 microns with exclusion from the 25 micron zone. **(C, F, I)** Peaked Axonal density versus vessel cross-sectional area for total axon count. Significant negative correlation was observed in the Schwann cell group (SC). Higher axonal densities were correlated with smaller vessels.

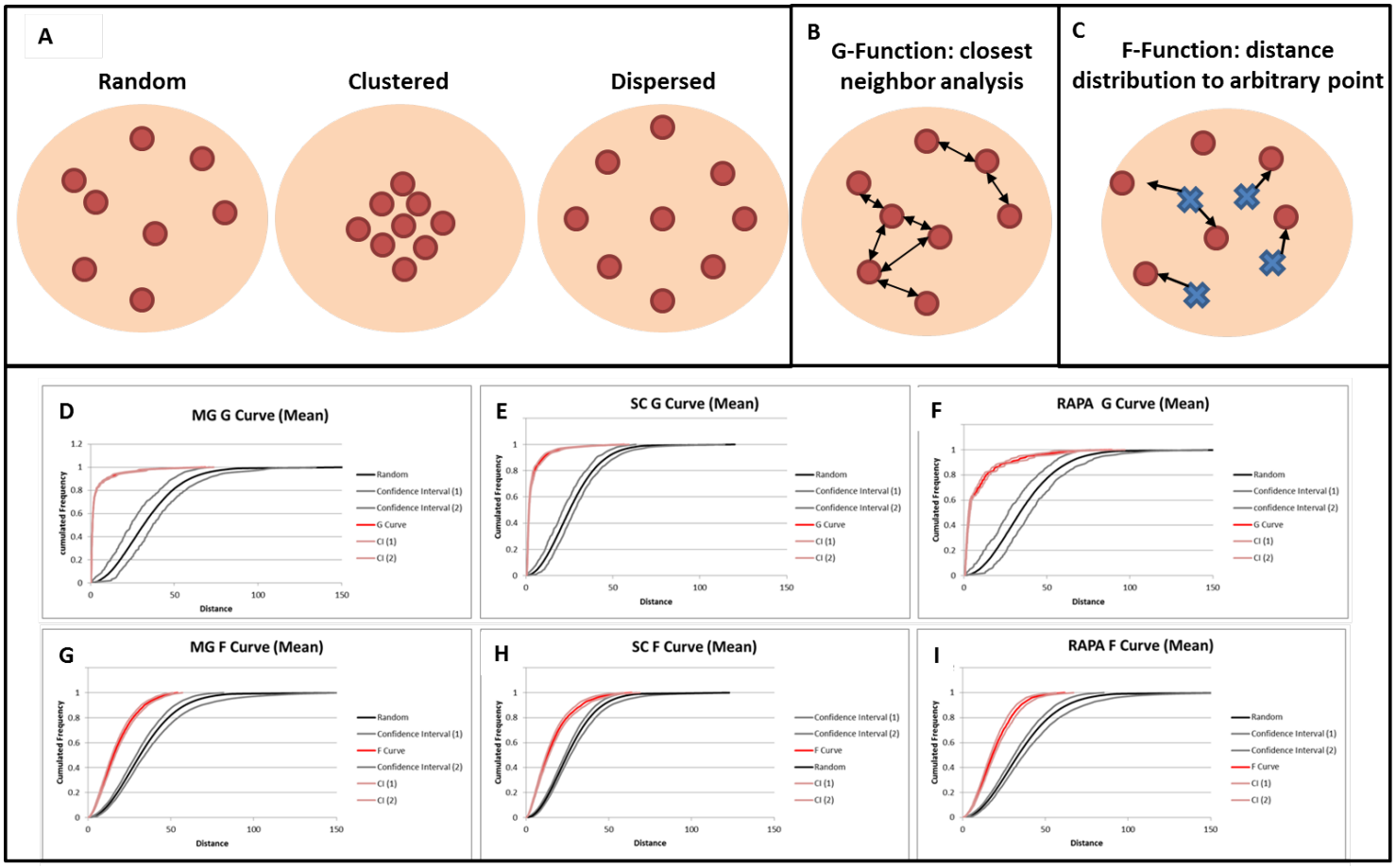

Figure 7: Analysis of axon clustering. (A) Axon distributions can be classified as random, clustered, or dispersed. **(B)** The closest neighbor analysis (G-function) measures the cumulative distance districutions between axons. **(C)** The F-function measures the distance distributions between an axon and an arbitrary point within the reference space. G-curve demonstrates that 90% of axons in the **(D)** Matrigel (MG) and **(E)** Schwann cell (SC) groups are fewer than 10 micros from each other. **(F)** Whereas those with rapamycin and Schwann cells (RAPA) are 16 microns apart. F-curve indicates a clustered distribution for axons in the **(G)** MG, **(H)** SC, and **(I)** RAPA groups.